Nuclear Inst. and Methods in Physics Research, A 974 (2020) 164170

Contents lists available at ScienceDirect

Nuclear Inst. and Methods in Physics Research, A

journal homepage: www.elsevier.com/locate/nima

Beam test calibrations of the HEPD detector on board the China Seismo-Electromagnetic Satellite

G. Ambrosi [a], S. Bartocci [b], L. Basara [c], R. Battiston [c,d], W.J. Burger [c], D. Campana [e], L. Carfora [f,b], G. Castellini [g], P. Cipollone [b], L. Conti [h,b], A. Contin [i,j], C. De Donato [b], F. De Persio [b], C. De Santis [b], F.M. Follega [c,d], C. Guandalini [j], M. Ionica [a], R. Iuppa [c,d], G. Laurenti [j], I. Lazzizzera [c,d], M. Lolli [j], C. Manea [c], M. Martucci [f,b], G. Masciantonio [b], M. Mergé [b], G. Osteria [e], L. Pacini [g], F. Palma [b], F. Palmonari [i,j], B. Panico [e], A. Parmentier [b], L. Patrizii [j], F. Perfetto [e], P. Picozza [f,b], M. Piersanti [b], M. Pozzato [j], M. Puel [c], I. Rashevskaya [d], E. Ricci [c,d], M. Ricci [k], S. Ricciarini [g], V. Scotti [e], A. Sotgiu [b], R. Sparvoli [f,b,*], B. Spataro [k], V. Vitale [b], S. Zoffoli [l], P. Zuccon [c,d]

[a] INFN Sezione di Perugia, V. A. Pascoli, 06123, Perugia, Italy
[b] INFN, Sezione di Rome "Tor Vergata", I-00133 Rome, Italy
[c] INFN - TIFPA, V. Sommarive 14, 38123 Povo (Trento), Italy
[d] University of Trento, V. Sommarive 14, 38123 Povo (Trento), Italy
[e] INFN - Sezione di Napoli, V. Cintia, 80126, Naples, Italy
[f] University of Rome "Tor Vergata", Department of Physics, I-00133 Rome, Italy
[g] IFAC-CNR, V. Madonna del Piano, 10, 50019 Sesto Fiorentino (Florence), Italy
[h] Uninettuno University, C.so V. Emanuele II, 39, 00186, Rome, Italy
[i] University of Bologna, V.le Berti Pichat 6/2, Bologna, Italy
[j] INFN - Sezione di Bologna, V.le Berti Pichat 6/2, Bologna, Italy
[k] INFN - LNF, V. E. Fermi, 40, 00044 Frascati (Rome), Italy
[l] Italian Space Agency, V. del Politecnico, 00133 Rome, Italy

ARTICLE INFO

Keywords:
Cosmic rays
Satellite
Particle detector
Calibration
Data analysis

ABSTRACT

CSES (China Seismo-Electromagnetic Satellite) is a Chinese-Italian space mission dedicated to monitoring of variations of the electromagnetic field and waves, plasma parameters, and particle fluxes induced by natural sources and artificial emitters in the near-Earth space. The satellite was launched from the Jiuquan Satellite Launch Center in the Gobi desert (Inner Mongolia, China) on 2, 2018. The expected mission lifetime amounts to 5 years.

The Italian contribution to the mission includes the design and construction of the High-Energy Particle Detector (HEPD), aimed to detect electrons in the energy range between 3 and 100 MeV and protons between 30 and 200 MeV, as well as light nuclei in the MeV energy range.

In this paper, we describe the calibration procedures applied to HEPD based on data acquired during two tests at accelerator laboratories, which were performed on HEPD Flight Model prior to the delivery to China for final integration. An additional acquisition of cosmic muons was performed in order to better characterize the detector response before launch.

1. Introduction

CSES (China Seismo-Electromagnetic Satellite) is a multi-disciplinary scientific mission led by the Chinese and Italian space agencies, and developed by the China Earthquake Administration (CEA) and the Italian National Institute for Nuclear Physics in collaboration with several Chinese, Italian and Austrian universities and research institutes [1].

The main objective of the mission is to investigate the coupling between lithosphere, atmosphere/ionosphere and magnetosphere, caused by a number of physical effects and interactions. Such phenomena are mostly caused by natural events, such as tropospheric activity (*e.g.*,

* Corresponding author at: University of Rome "Tor Vergata", Department of Physics, I-00133 Rome, Italy.
E-mail address: roberta.sparvoli@roma2.infn.it (R. Sparvoli).

https://doi.org/10.1016/j.nima.2020.164170
Received 5 February 2020; Received in revised form 13 May 2020; Accepted 15 May 2020
Available online 28 May 2020
0168-9002/

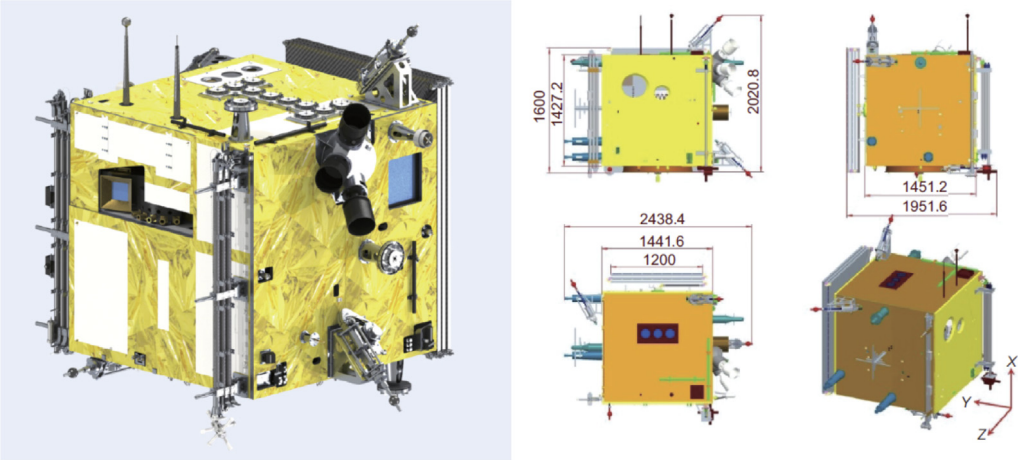

Fig. 1. Layout of the CSES satellite: the main body has size 145 cm (Y) × 144 cm (Z) × 143 cm (X), which increases after the deployment of the solar panel and booms.

lightnings) and volcanoes, as well as by anthropogenic electromagnetic emissions. In addition, electromagnetic disturbances associated with seismic activity can induce ionospheric perturbations and possible precipitation of particles from the inner Van Allen belts [2–4]. To this purpose, the mission has been conceived to take advantage of a multi-instrument payload comprising eight detectors for the measurement of electromagnetic field components, plasma parameters and energetic particles, as well as X-ray flux.

Another important scientific goal of the mission is to study specific space-weather phenomena triggered by solar-terrestrial interactions, as well as cosmic-ray propagation. In particular, CSES mission is monitoring solar activity of both transient (Solar Energetic Particle, or SEP, emission) and secular nature (solar modulation), by detecting protons and electrons from a few to hundreds of MeV. These measurements will add information on particle spectra in the MeV region for the ongoing 24th solar cycle, currently monitored directly by ACE [5], SOHO [6], Stereo [7,8], Parker Solar Probe [9] and AMS-02 space experiments [10,11] in different energy windows, and previously by PAMELA [12,13]. In this context, the High-Energy Particle Detector was designed and built by the Italian collaboration in order to ensure the highest-quality measurements of charged particles at energies between 3 and 100 MeV for electrons and between 30 and 200 MeV for protons.

During the final assembly phase, and before delivery to China, the Flight Model of HEPD was beam tested (electrons and protons) at various facilities (see Section 3). In addition, the instrument was exposed to the acquisition of cosmic rays (atmospheric muons) in clean rooms at Roma Tor Vergata Division of the National Institute of Nuclear Physics (INFN) in Rome (Italy) between October and November 2016. Such tests were aimed to characterize the energetic response of the detector, necessary for in-flight particle-flux reconstruction.

The article is organized as follows: after an overview of the CSES mission and HEPD instrument (Section 2), two beam tests, carried out on HEPD Flight Model before satellite launch, are described in Section 3. In particular, an electron beam test at the INFN-LNF Beam Test Facility and a proton beam test at the Trento Proton-Therapy Center are illustrated in Sections 3.2 and 3.3, respectively. Section 4 is dedicated to Monte Carlo simulations of the apparatus and their comparison to beam test data. Finally, in Section 5, we report methods and results of energy calibrations on HEPD silicon tracker and calorimeter. We draw our conclusions in Section 6.

2. CSES mission and HEPD Detector

CSES is the first element of a multi-satellite monitoring system including several missions scheduled for the next few years, designed to investigate the top side of the ionosphere by means of the most advanced techniques and equipment, and able to gather worldwide data of the near-Earth electromagnetic and particle environment.

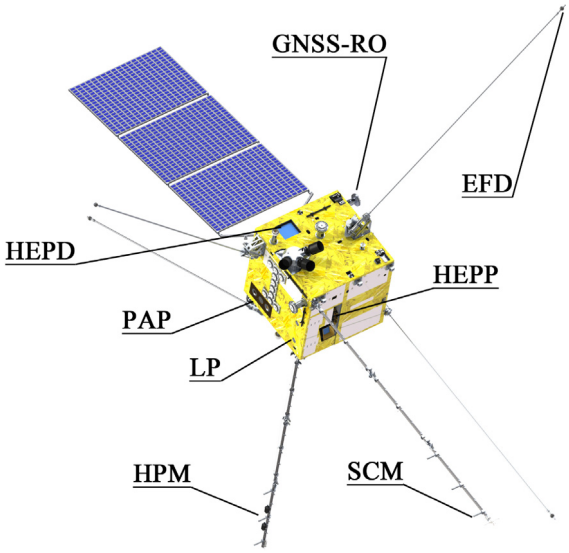

Fig. 2. Instrument position on board CSES: in orbit configuration is shown, as can be deduced by deployed solar panel and booms.

The satellite, based on the Chinese 3-axis stabilized CAST2000 platform, has a mass of about 700 kg and was placed into a sun-synchronous orbit at a 507 km altitude, with a 97° inclination and a periodic 5-day ground track. In its launch configuration, CSES main body (Fig. 1) has size 145 cm (Y) × 144 cm (Z) × 143 cm (X), which increases after the deployment of the solar panel and booms.

The satellite has two distinct working regions, in order to reduce any interference on the scientific payloads from solar panel rotation or attitude adjustments. One region lies in the geographical latitude range between −65° and +65°, where data are collected and transmitted, while the platform adjustment zone, where all the payloads are switched to standby mode, is found at latitudes > +65° or < −65°. Such operating mode of the satellite does not affect much the observational capabilities of HEPD, thanks to its large angular aperture and the tilted magnetic field configuration; the rigidity cut-off accessible to the instrument at latitudes close to ± 65° and longitudes near 80° and 220° is indeed sufficiently low (mostly on southern hemisphere), allowing the instrument to register galactic and solar particles down to the lower energy limit of the instrument for a fair amount of time.

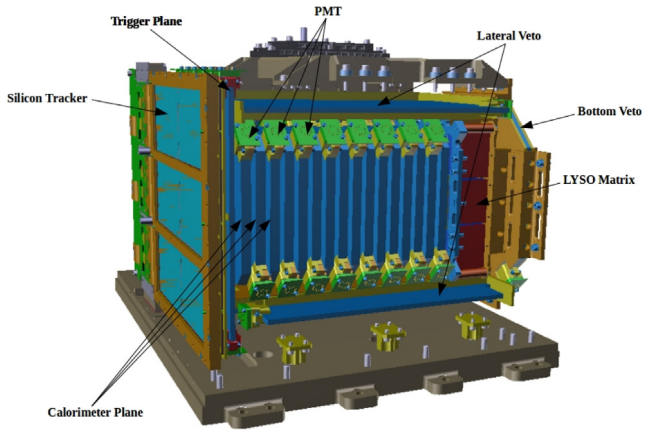

Fig. 3. CAD model of the HEPD apparatus: lateral and top panels have been removed for visualization purposes.

Table 1
Main specifications of the High Energy Particle Detector HEPD.

Mass (kg)	45
Dimensions (cm^3)	40.36 × 53.00 × 38.15
Power consumption (W)	<40
Energy window (MeV)	protons: 30 ÷ 200 electrons: 3 ÷ 100
Geometric factor (cm^2sr)	410 (protons at 100 MeV) 355 (electrons at 20 MeV)

Eight scientific payloads are installed on board CSES [14–18] as illustrated in Fig. 2: namely, a High-Precision Magnetometer (HPM) to measure both the intensity and three components of the magnetic field in the low frequency range (60 Hz); a Search-Coil Magnetometer (SCM) for measuring the three components of the magnetic field at higher frequencies; an Electric Field Detector (EFD), including four probes installed on as many booms, aimed at the measurement of the three components of the electric field; a Plasma Analyzer Package (PAP) and a Langmuir Probe (LP) to observe ion/electron density and temperature, ion drift velocity and plasma composition; a Global Navigation Satellite System (GNSS) Occultation Receiver for studying the ionospheric plasma profile; and two particle detectors, the High-Energy Particle Package (HEPP) and the High-Energy Particle Detector (HEPD), for measuring high-energy charged particles and X-ray flux.

2.1. The HEPD instrument

The High-Energy Particle Detector was developed by the Italian branch of the CSES mission. A computer-aided design (CAD) model of the HEPD apparatus – with lateral and top panels removed – is shown in Fig. 3.

The HEPD detector is contained in an aluminum box with size 40.36 ×53.00× 38.15 cm^3. Total mass is about 45 kg, while power consumption depends on the status of HEPD, but is always lower than 30 W. Table 1 presents HEPD main characteristics.

From top to bottom, the apparatus is made up of the following subdetectors:

- a tracking system, including two double-sided silicon microstrip planes (1 cm far from each other), with size 213.2 mm × 214.8 mm × 0.3 mm excluding mechanics. Each silicon plane is divided into three identical independent sections, each one containing two silicon sensors;
- a trigger system, consisting of one EJ-200 plastic scintillator layer segmented into six paddles. Any paddle size is 20 cm × 3 cm × 0.5 cm, and readout is performed by two Photo-Multiplier Tubes (PMTs);
- a range calorimeter composed of two sections. The upper part is a tower of 16 EJ-200 plastic scintillator planes (15 cm × 15 cm × 1 cm), each one read out by two PMTs. The lower part is a 3 × 3 matrix of LYSO (Lutetium-Yttrium Oxyorthosilicate) inorganic scintillator crystals. Each crystal (5 cm × 5 cm × 4 cm) is read out by a single PMT located on its bottom side;
- an anti-coincidence (VETO) system composed of five EJ-200 plastic scintillator planes (0.5-cm thick), each one read out by two PMTs.

All plastic scintillators and crystals are wrapped in a layer of aluminized Mylar. Scintillator readout (both EJ-200 plastics and LYSO crystals) is performed by R9880U-210 Hamamatsu PMTs.

Along one side of the sensitive block, two main sub-systems are placed to complete the instrument:

- an electronic sub-system made of four boards for trigger management, data acquisition, On-Board Data Handling (OBDH), housekeeping and low-voltage power distribution [19];
- a Low-Voltage Power Supply (LVPS) sub-system, developing into two low-voltage power lines from the satellite power bus and a High-Voltage Power Supply (HVPS) system providing two high-voltage lines for Silicon Detector and PMT bias.

In order to avoid permanent failures, each sub-system (electronic boards and power supplies) is duplicated in a HOT (MAIN) and COLD (SPARE) side for redundancy. Additional technical details about HEPD subdetectors and electronics are reported in [20].

Following a standard space model philosophy, four HEPD models were produced and fully integrated in the clean rooms at Roma Tor Vergata Division of the National Institute of Nuclear Physics (INFN) in Rome:

- The Electrical Model (EM), used to verify the electric and electronic interfaces between payload and spacecraft;
- the Structural Thermal Model (STM), constructed to validate structural and mechanical design, as well as thermal control system;
- the Qualification Model (QM), used to qualify all sub-systems by stress tests, as well as to calibrate the instrument and assess its compliance with space-environment and magnetic-cleanliness standards;
- the Flight Model (FM) – space qualified, calibrated and tested to verify its compliance with specifications – which was finally shipped to the DFH Satellite Company, Ltd., in Beijing (China) in December 2016.

CSES was launched in February 2018 and is in data-taking mode since then. Some performance of the HEPD in flight were reported in [20]. Analysis on galactic protons and electrons are on-going, while no SEP events were detected by the instrument so far. In Fig. 4 we show the capability of HEPD in detecting changes in particle populations following geomagnetic storms while flying along the orbit. Data refer to the storm occurred in late August 2018. From the picture it is clearly visible how the external electron belt is considerably populated after the impact of the storm (right panel) with respect to a few days before (left panel). The detector is switched off when passing over polar caps (± 65 degrees of latitude).

In Fig. 5 we show a single semi-orbit of CSES-01 (upper panel), with the corresponding proton (squares) and electron (open circles) time profiles along such semi-orbit (lower panel). The passage over a peripheral sector of the SAA is visible from the increase in the proton counting rate. Our acquisition rate over the energy acceptance window is continuous both in electrons and in protons between ± 65 degrees of latitude.

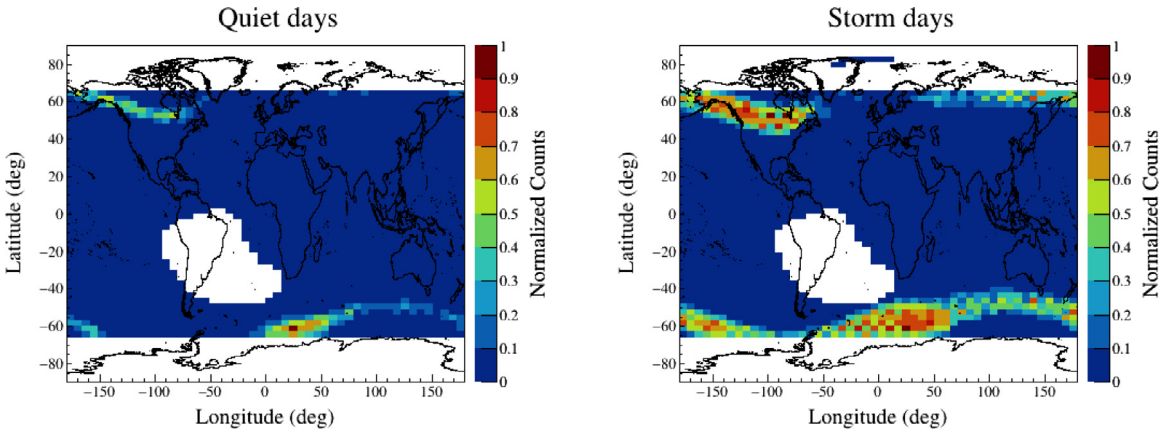

Fig. 4. Change in the low energy electron population inside the outer radiation belts as a result of the 2018 August geomagnetic storm (right panel) with respect to a few days before (left panel) (color online).

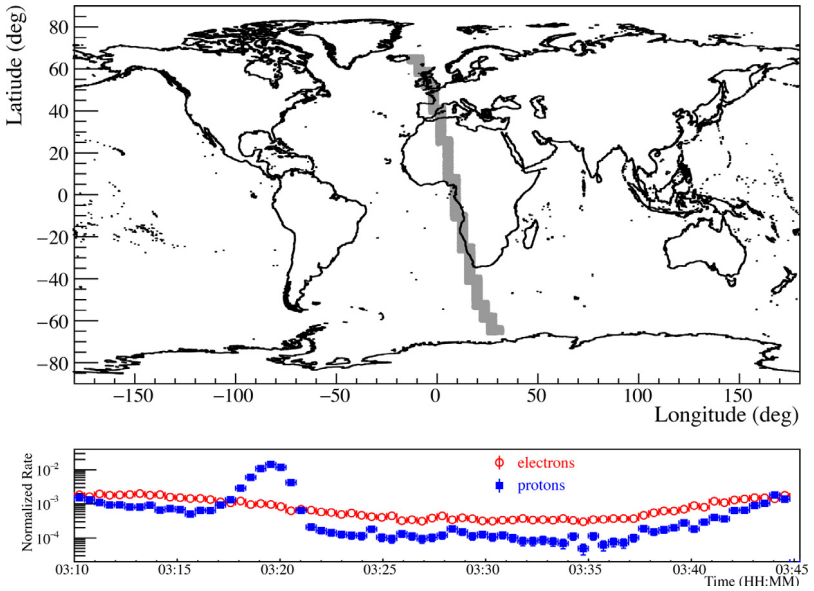

Fig. 5. A single semi-orbit of the CSES-01 satellite (upper panel), together with proton (blue squares) and electron (red open circles) time profiles along such semi-orbit. The acquisition of both populations is continuous and the passage over the SAA is evident by the rise in proton counting rate.

3. Energy calibration of the HEPD Flight Model

In October 2016, at the INFN-LNF Beam Test Facility (Frascati, Italy), HEPD was exposed to electron beams of 30, 45, 60, 90 and 120 MeV, while, in November 2016 at the Trento Proton-therapy Center (Trento, Italy), proton beam tests at 37, 51, 70, 100, 125, 154, 174, 202, and 228 MeV were performed. Finally, several acquisitions of cosmic muons were done right before the final delivery to China (December 2016).

All HEPD tests were performed with the support of the Electrical Ground Support Equipment (EGSE) that emulates the satellite by providing power to HEPD, sending telecommands used for detector configuration, and receiving telemetry and scientific data. Fig. 6 shows the interface of the EGSE program used to send telecommands.

3.1. Muon acquisition and PMT signal equalization

Atmospheric muons data were used to equalize the PMT responses to Minimum Ionizing Particles (MIPs). Indeed, since a MIP is expected to release the same energy amount in any plane, atmospheric muon data allow to equalize PMT signals by correction for different PMT gains, optical-couplings to scintillators and collection efficiencies.

The equalization of the calorimeter PMT responses is the first stage of released energy reconstruction in any scintillator plane starting from raw ADC counts. Indeed, the PMTs located in the scintillator tower may show different responses to the same amount of deposited energy, because of differences in scintillation efficiencies and gain, or fluctuations in light collection. Therefore, an equalization procedure must be applied in the offline analysis phase, by studying the individual response of each PMT to the same input energy, as in the case of a passing MIP. To this purpose, cosmic muon data were collected by using both COLD (October 2016) and HOT (November 2016) sides of HEPD electronics. After subtracting the pedestal from the raw ADC signal of each channel, vertical muon events passing through the entire apparatus were selected.

When vertical events are selected, any two PMTs placed at opposite corners of any plane are expected to approximately collect equal amounts of photons. For large event numbers, any difference in signal distributions from the couple PMTs will be only due to different gains.

A Landau function was fitted to any MIP signal distribution, and the most probable value was used as a coefficient to weight the signal in any given PMT. The equalization coefficient K_i^{EQ} of the ith PMT was obtained by scaling of the corresponding peak to the arbitrary value of

Fig. 6. EGSE: Electrical Ground Support Equipment, emulating the satellite, to manage HEPD configuration and acquisition (right). Screenshots of System Control and Configuration Telecommands are shown (left).

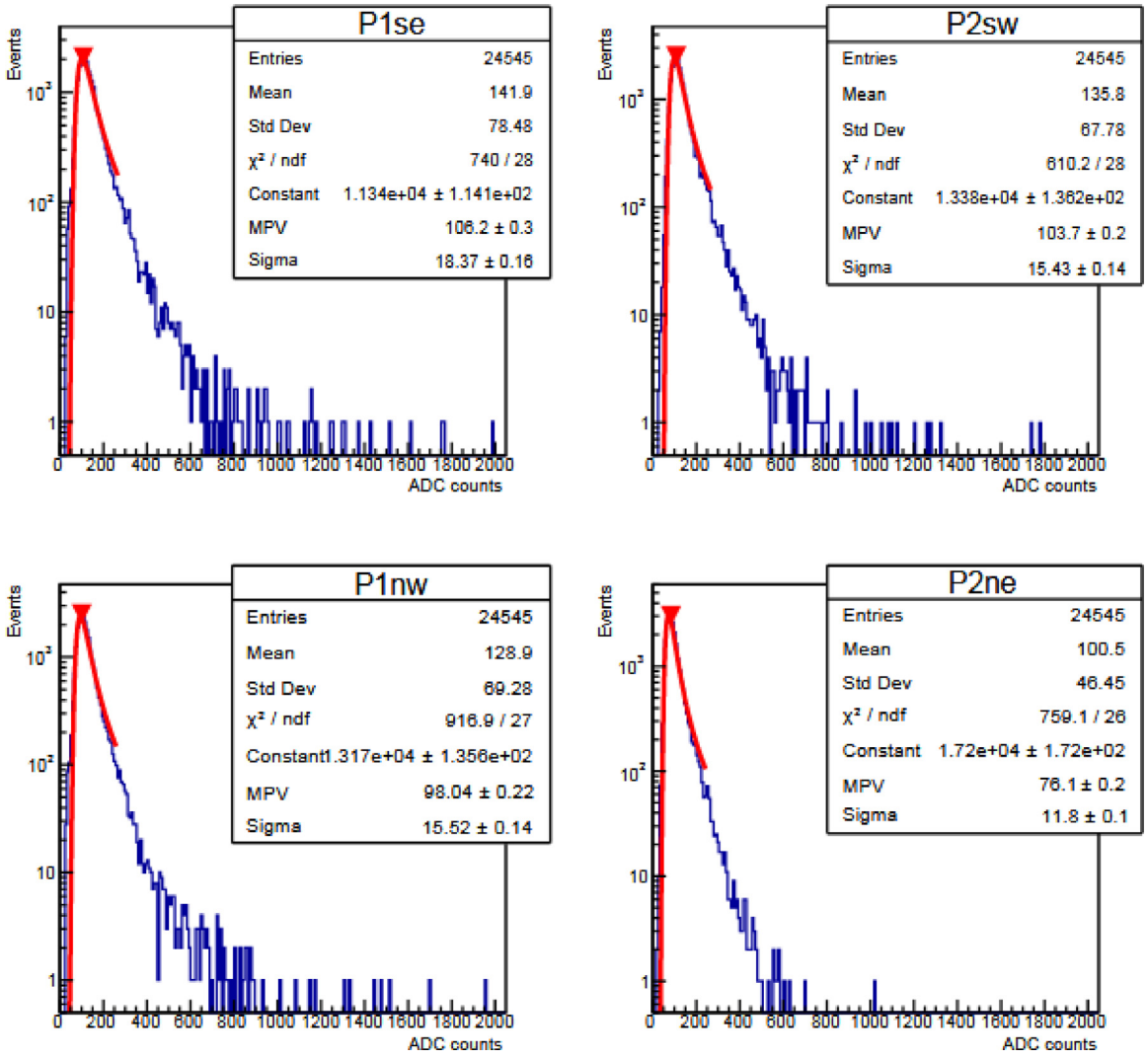

Fig. 7. A sample of muon signal distributions for HEPD PMTs (the four ones lying in the first two calorimeter planes): for any PMT of the apparatus, the most probable value (MPV) from Landau fit was used to retrieve the corresponding equalization factor. The "se" label stands for south-est, "sw" for south-west, "ne" for north-est, and "nw" for north-west. All labels are related to the positions of the PMTs.

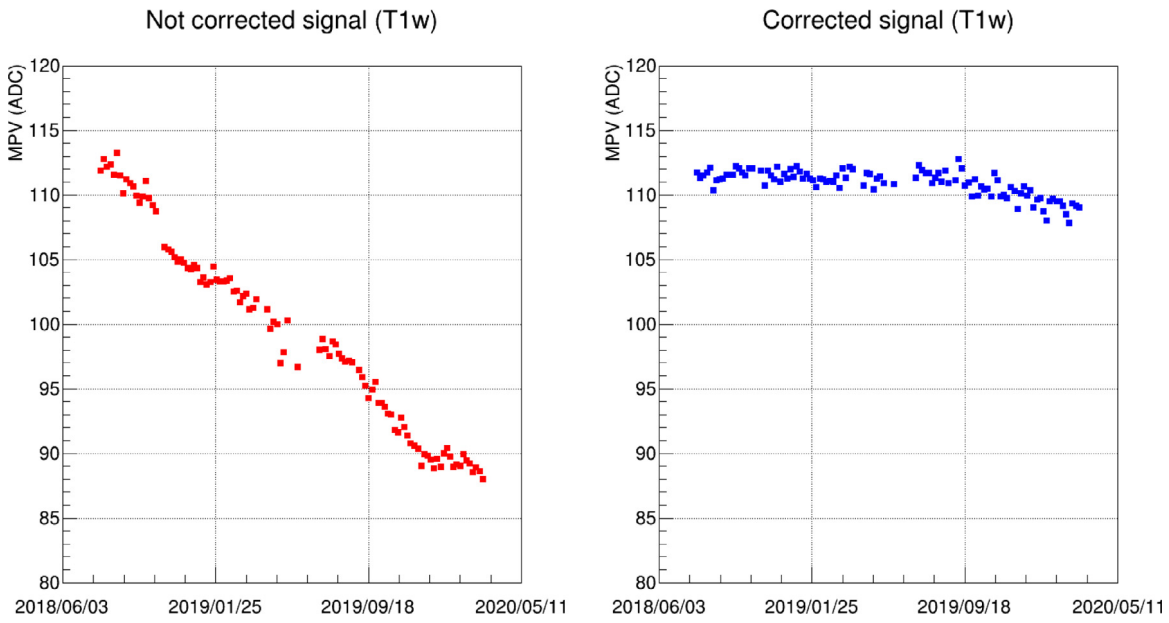

Fig. 8. Off-line PMT signal correction: example of the correction procedure for one PMT of the trigger paddle T1 (T1 west). Left: signal before correction, over the period from August 2018 to March 2020. Right: corrected signal.

200 ADC counts, as follows:

$$K_i^{EQ} = \frac{200}{MPV_i}, \tag{1}$$

where MPV_i is the most probable value obtained from the Landau fit of the ADC signal distribution. In Fig. 7, the ADC signal distributions and corresponding Landau fits for the four PMTs of the first two calorimeter planes are reported. Once any K_i^{EQ} equalization factor was estimated, the raw ADC signals were equalized on an event-by-event basis, according to the following formula:

$$S_i^{EQ} = K_i^{EQ} S_i^{RAW}, \tag{2}$$

where S_i^{RAW} is the raw signal measured for the ith PMT, and S_i^{EQ} is the same signal after equalization.

Once the PMT signal equalization is performed, beam tests allow to calibrate the energy response of the whole detector by provision of the calibration curve for the ADC-energy conversion to be used for energy reconstruction.

Since launch, continuous monitoring of PMT equalization was performed by a check of the time stability of the MIP peaks.

HEPD is not capable to select a clean MIP sample in orbit because it is not designed to detect high-energy protons not fully contained inside the calorimeter. What can be done is to select a sample of passing-through particles that do not interact inside the detector, do not touch the lateral veto and with an energy deposit which is as close as possible to that of a MIP particle.

This MIP-like signal distribution (in ADC channels) for each PMT is then fitted by a Landau function and the most probable values (MPVs) and the widths are plotted as a function of time. Fig. 8 (left) shows for example the MPVs obtained for one PMT from the trigger paddle T1, during the period from August 2018 to March 2020. A decrease in the signal, probably due to the aging of the PMT and the scintillator paddle, can be noticed.

In order to take into account this effect, an off-line correction is applied for each PMT. The MPVs of the MIP-like distributions are calculated every 5 days for each PMT i, then the correction factor K_i^{MIPcal} at time t is calculated as follows:

$$K_i^{MIPcal} = \frac{MPV_i^{first-on}}{MPV_i^{t}}$$

where $MPV^{first-on}$ are the MPVs obtained with one acquisition of MIP-like events taken immediately after the first power-on of the detector in orbit. The corrected signal of each PMT is then given by:

$$S_i^{corr} = K_i^{MIPcal} * S_i^{EQ}$$

The correction effect applied to the same PMT of the trigger paddle T1 can be seen in Fig. 8 (right). Same procedure is repeated for every PTM of the instrument.

3.2. Electron beam tests at INFN-LNF Beam Test Facility (BTF)

The scope of the measurements performed at the Beam Test Facility at INFN-LNF in Frascati was to calibrate the HEPD Flight Model, to test detector functionality, and to assess and characterize HEPD's detection performance for electrons at different energies. In addition, the satellite communication interfaces were tested using the Electrical Ground Support Equipment.

The BTF[1] is an experimental area for detector testing and diagnostics, designed for production of electron and positron beams. The facility is a part of the DAFNE accelerator at the INFN National Laboratories of Frascati.

The LINAC-based installation produces packets of electrons and positrons at a frequency of 50 pulses per second and with an intensity that can be modulated between 10^7 and 10^{10} particles per bunch, in the energy range 300–750 MeV for electrons and 300–550 MeV for positrons. Typically, the LINAC injects these beams into the accumulation ring of DAFNE, setting the working energy at 510 MeV.

A pulsed magnet deflects the beam into a transfer line, which carries it to the BTF experimental area, equipped with diagnostic tools; the beam can be intercepted by a *Cu* target with variable thickness, which strongly attenuates beam intensity. The outgoing beam acquires a broadened energy spectrum down to 30 MeV. The remaining transfer line is composed of various magnetic dipoles, quadrupoles, correctors and couples of vertical and horizontal scrapers. These elements act as energy and multiplicity selectors.

[1] http://www.lnf.infn.it/acceleratori/btf/.

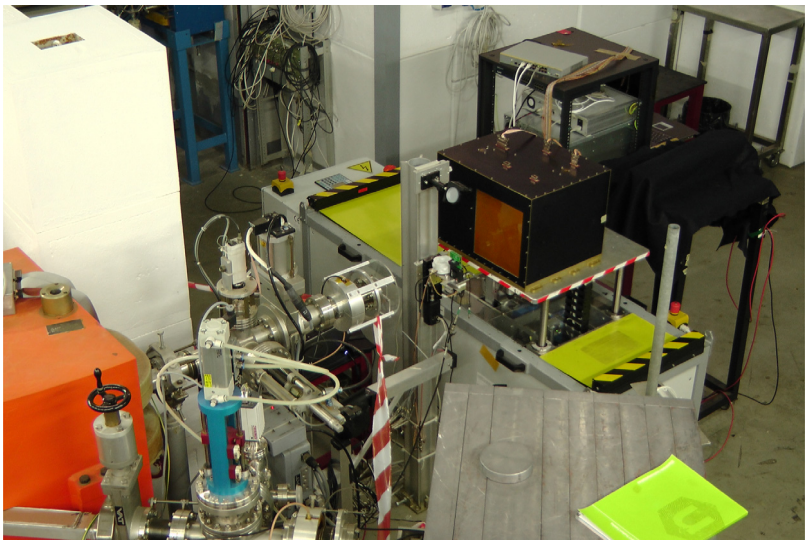

Fig. 9. HEPD setup at BTF: HEPD – the black box with the orange window in correspondence to the active detector – placed on the movable platform in front of the beam is connected to the EGSE; the Medipix and calorimeter provided by BTF staff for beam monitoring are visible on the front and back side of HEPD, respectively. (For interpretation of the references to color in this figure legend, the reader is referred to the web version of this article.)

3.2.1. BTF setup

BTF line parameters were optimized to obtain beam bunches of low multiplicity (ideally 1 electron) at different energies: 120 MeV, 90 MeV, 60 MeV, 45 MeV and 30 MeV.

Bunch frequency spanned the range from 49 Hz (when DAFNE was not operating) down to 18 Hz (for positron primaries and DAFNE on operation). The bunches contained 0, 1, or > 1 electrons according to a Poisson distribution. A couple of remotely operated calorimeter (beam-spectrum and multiplicity monitor) and *Si* pixel imaging detector of the Medipix family (beam spot monitor) were used in order to check electron content distribution of the bunches and beam spot size, respectively.

A movable platform was used, which could be translated horizontally and vertically with a precision of 0.2 mm. The detector was placed on the platform with the incident beam located at the very center of HEPD window by laser pointing (Fig. 9).

HEPD was connected to the EGSE in order to remotely manage detector configuration and acquisition. The tests were performed at different incident beam positions, with different trigger masks and VETO settings, as well as different PMT thresholds. All measurements were done with the beam perpendicular to HEPD window, except for a few runs where the inclination between the beam and the instrument was $\pm 7°$, to test the efficiency of the lateral VETO. Acquisitions of electrons were interspersed in beam-off calibration runs to evaluate and monitor electronic noise (pedestal mean and RMS).

3.3. Proton beam tests at Trento Proton-Therapy Center

The aim of these measurements was to assess and characterize HEPD's performance in proton detection.

The Trento Proton-Therapy Center is a unique, cutting-edge therapy facility in Italy for treatment of patients affected by solid cancers, in two rooms equipped with rotating gantries. A third room, which accommodates a horizontal beamline, is totally dedicated to research in collaboration with the Trento Institute for Fundamental Physics and Applications (TIFPA[2]). Protons are delivered to the facility by a superconducting cyclotron operating at an energy spanning the interval from 70 to 228 MeV, with a rate of up to 10^9 particles per second.

[2] http://www.tifpa.infn.it/sc-init/med-tech/p-beam-research/.

3.3.1. Beamline setup

Proton beams with different energies were used at rates below 1 kHz. The low rate condition was achieved by putting the proton source in dark current mode inside the cyclotron. The high voltage of the source was set below the threshold commonly used for standard operations, resulting in low-energy proton fluxes; yet, at these low rates, devices along the beam line are not efficient, resulting in larger energy, pointing and rate fluctuations of the beam.

HEPD was placed in front of the beam on a movable platform whose horizontal placement was remotely controlled, while vertical translation was performed manually (Fig. 10). The incidence point of the beam was set at the very center of HEPD window by laser pointing. Also beam orthogonality was checked using a laser. An auxiliary scintillator, read out by a Micro Channel Plate, was placed along one side of HEPD at beam height in order to check beam rate and energy.

As for electron beam tests, HEPD was connected to the EGSE in order to remotely change detector configuration and manage acquisition.

HEPD was tested by means of proton beams of different energies (37, 51, 70, 100, 125, 154, 174, 202, and 228 MeV), at different incident beam positions, in different operating modes. Once again, proton acquisitions were periodically interspersed in beam-off calibration runs in order to evaluate and monitor electronic noise.

4. Monte Carlo simulations

A Geant4-based Monte Carlo (MC) program [21] was developed to simulate physics processes and detector response. The Geant4 model is almost identical to HEPD model from CAD, including all sensitive subdetectors and most mechanical support structures. HEPD simulation model in wire frame visualization is shown in the left panel of Fig. 11.

The Geant4 simulation employed G4 Standard EM Physics option4 for the electromagnetic interactions, whereas G4IonElasticPhysics, G4IonQMDPhysics, G4HadronElasticPhysics e G4HadronPhysicsShielding were used for the hadronic interactions.

The MC code was extensively used to simulate the experimental setups arranged during electron and proton beam tests. Both detector and incident beam configurations (*i.e.*, beam energy, spot size, incidence position on HEPD window, etc.) were accurately reproduced, in order to fine-tune simulated data with beam test data. As an example, in Fig. 12 the simulation of the passage of proton beams through the HEPD apparatus is shown, along the lines of Trento Proton-Therapy

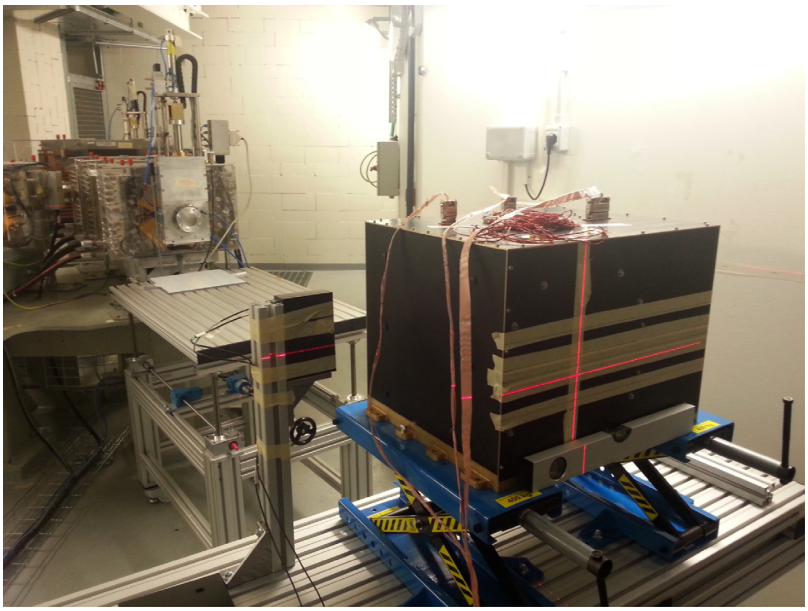

Fig. 10. HEPD setup at the Trento Proton-Therapy Center: HEPD was placed on a movable platform with the incident beam located at the center of HEPD window by laser pointing.

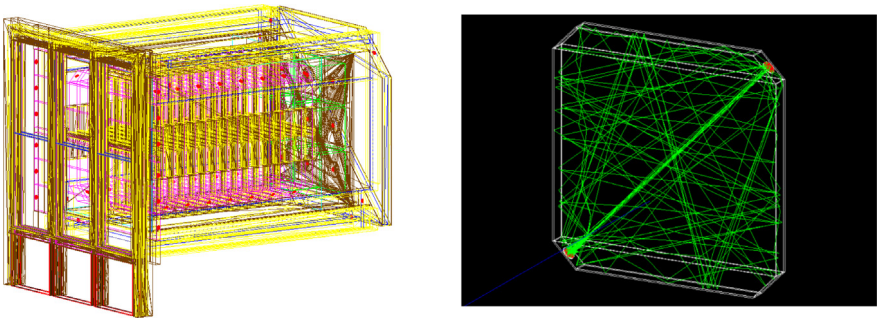

Fig. 11. Monte Carlo simulations of the HEPD apparatus: the HEPD simulation model in Geant4 wire frame visualization (left) contains a detailed representation of detector geometry, including all sensitive sub-detectors and most mechanical support structures. The Monte Carlo simulation of light propagation in any HEPD calorimeter plane from a 50-MeV electron event is shown in the right image. The two red circles represent PMTs where the number of photo-electrons is estimated. (For interpretation of the references to color in this figure legend, the reader is referred to the web version of this article.)

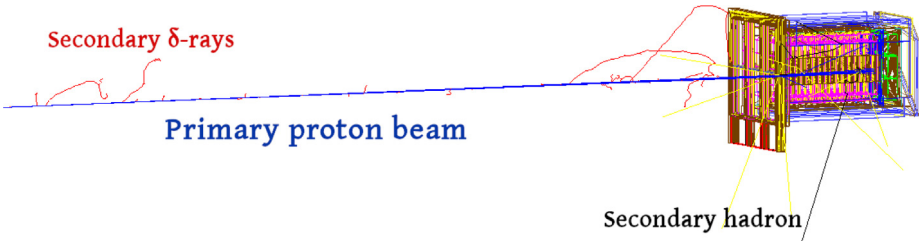

Fig. 12. Monte Carlo simulation of a 200-MeV proton beam through HEPD at the Trento Proton-Therapy Center: the red tracks are delta rays produced along the paths of the beams in air (186 cm long), while the black line is a secondary hadron produced in the interaction. (For interpretation of the references to color in this figure legend, the reader is referred to the web version of this article.)

beam tests. The red tracks represent delta rays produced along the paths of proton beams in air (186 cm long).

Light propagation inside each calorimeter plane was implemented in the simulation as well, in order to obtain the number of photo-electrons collected by each PMT (right panel of Fig. 11) for any given primary energy. This information was then used to "digitize" the Monte Carlo output for all PMTs in the calorimeter, that is, converting PMT responses from photo-electron numbers into ADC counts. The same procedure was followed for the digitization of the LYSO calorimeter.

To this purpose, for each beam energy, a Gaussian function was fitted to the ADC signal distribution from each PMT (after pedestal subtraction and equalization), and the same was done for any photo-electron distribution obtained from Monte Carlo. Mean values from Gaussian fits were then used to produce calibration curves (one for each PMT) for conversion of photo-electrons into ADC counts.

Fig. 13 shows the two above-mentioned distributions obtained using a 100-MeV proton run for the south-east PMT of the third calorimeter plane (P3se). The corresponding calibration curve is reported in Fig. 14. Black asterisks correspond to a set including a cosmic-muon run, a

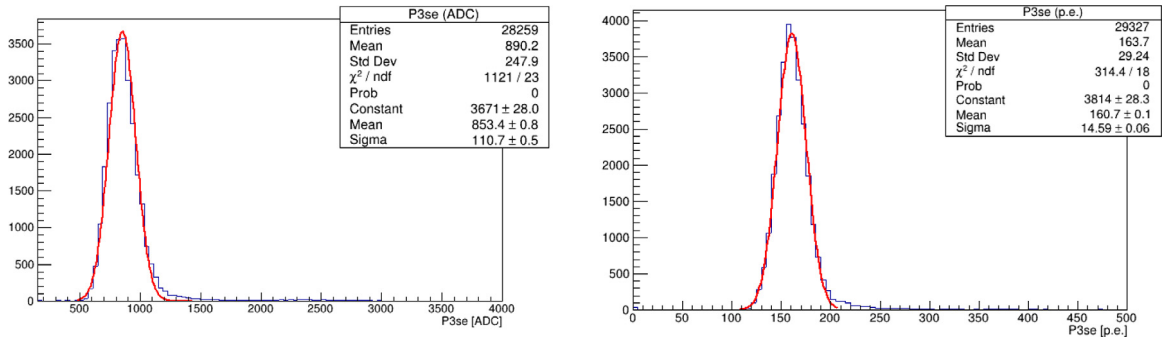

Fig. 13. Distributions from a 100 MeV proton run for the south east PMT of the third calorimeter plane (P3se): the ADC signal distribution for P3se from the beam test data (left) and the photo-electron distribution in P3se from the Monte Carlo simulation (right).

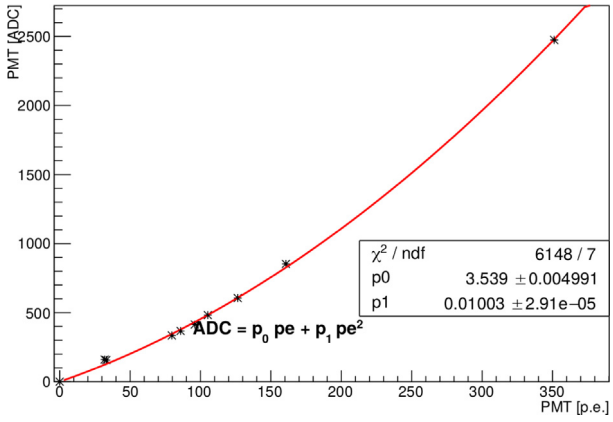

Fig. 14. Conversion curve from photo-electrons into ADC counts for the P3se PMT: the black asterix points correspond to a cosmic muon run, a 30 MeV electron run and seven proton runs (70, 100, 125, 154, 174, 202 and 228 MeV).

30 MeV electron run and seven proton runs (70, 100, 125, 154, 174, 202, and 228 MeV).

Fig. 15 – showing ADC signal distributions obtained from a 51-MeV proton run and compared to simulation – is a proof of successful digitization, being the agreement very good.

5. Results

5.1. Silicon tracker energy calibration

In order to accomplish tracker energy calibration, several data – namely, proton runs taken at Trento Proton-Therapy Center and atmospheric-muon runs – were exploited over a wide $\beta\gamma$ range.

5.1.1. Calibration of the strip signal

Particle energy loss ($\frac{dE}{dx}$) is reconstructed starting from the ADC signal collected by the silicon micro-strips contained in the tracker ladders. To the purpose of signal reconstruction, it is crucial to identify a stable calibration procedure in order to produce and subtract pedestals from raw data, and to define spread in each channel (4608 channels overall). To perform such a calibration, runs in which no signal is present are required. They are used to compute the following two quantities:

1. channel pedestal

$$p_i = \frac{1}{N_{events}} \sum_{j=0}^{N_{events}} ADC_{ij}$$

2. channel sigma

$$\sigma_i = \sqrt{\frac{1}{N_{events}} \sum_{j=0}^{N_{events}} (ADC_{ij} - p_i)^2}$$

where i is the channel index, from 0 to $N_{chann} - 1$, and j the event index. σ_i is called the *raw noise*, and represents the individual channel fluctuation; therefore, it is computed for each channel. The calculation of raw noise is also used to mask dead (too low σ_i) and noisy channels (too large σ_i).

An additional fluctuation exists (*common mode noise*), which must be subtracted from the readout signal ADC_{ij}. This noise, which is common to all 64 readout channels of the same VA chip, is related to the preamplifier chip and can be calculated as follows:

$$CN_j = \frac{1}{N_j} \sum_{i=0}^{VA_{chann}} (ADC_{ij} - p_i).$$

The result of this additional signal conditioning is a calibrated signal with corresponding p_i and σ_i^{ped} parameters for each channel, where σ_i^{ped} is calculated as:

$$\sigma_i^{ped} = \sqrt{\frac{1}{N_{events}} \sum_{j=0}^{N_{events}} (ADC_{ij} - p_i - CN_i)^2}$$

5.1.2. η-correction for the floating strips

Once data are pedestal – and common-noise subtracted, and σ_i^{ped} is known for every i, it is possible to identify hit strips with appropriate signal-above-noise thresholds. At first, "cluster multiplicity" - *i.e.,* the number of adjacent silicon strips with a signal-above-noise threshold that mark particle passage – was studied at different beam energies. Fig. 16 shows that cluster multiplicity is always 1 or 2 for all beam energies. At low energy, there is a probability of $\sim 50\%$ to have clusters composed by 1 or 2 strips. Conversely, at high energy most clusters seem to be composed by only 1 strip.

This behavior can be explained considering the silicon detector structure discussed in the Appendix of [20]: not all the strips are directly connected to the read-out electronics, but rather an alternation of read-out and floating strips exists. At low energy, the charge deposited in the detector by any particle is high, and the signal on the strips adjacent to the "seed" (*i.e.*, the strip marked by the highest deposit, which can be therefore considered as the closest to particle trajectory) is above threshold even when the particle crosses a floating strip. Since read-out and floating strips are present in the same number, a 50% probability of a multiplicity equal to 1 is expected when the particle trajectory is close to a read-out strip that collects all its charge. On the other hand, a 50% probability of a multiplicity equal to 2 is also expected when the particle trajectory is close to a floating strip, and its charge is collected by the two adjacent read-out strips by means of capacitive coupling effects. Ideally, the charge collected on the neighboring read-out strips via inter-strip capacitance C_s is $Q/2$, where

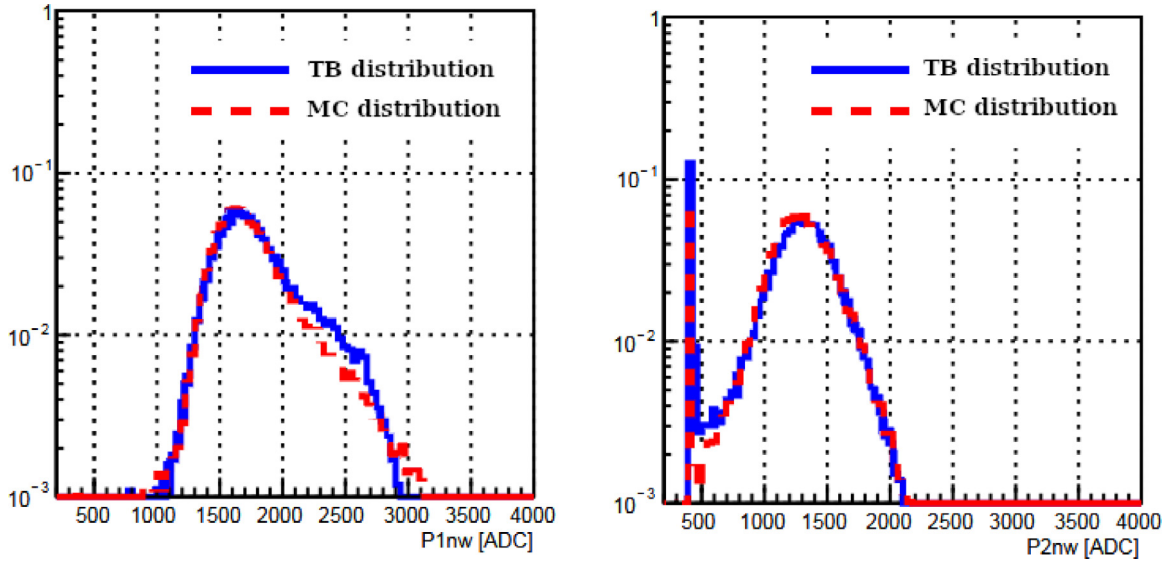

Fig. 15. ADC signal distributions from proton beam test data (TB blue continuous curve) and digitized Monte Carlo simulation (MC red dashed curve): the two distributions for the P1nw (left) and P2nw (right) PMTs correspond to a 51-MeV proton run.

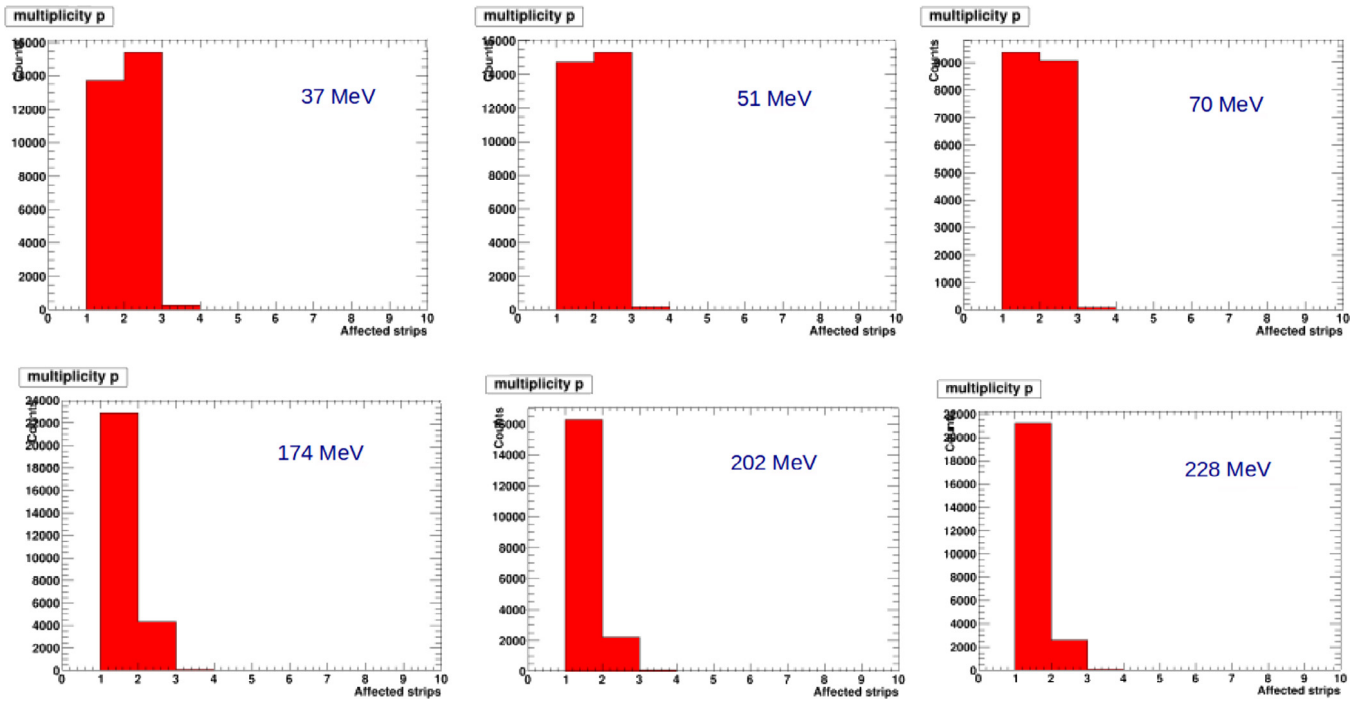

Fig. 16. Histogram of cluster-multiplicity variation for the P side of the central ladder at different proton beam energies: the number of strips interested in the cluster is found along the X direction.

Q is the charge released on the floating strip. However, in a more realistic situation, the probability of charge loss increases if the particle hits the floating strip, and it must be considered and corrected for.

Thus, back to Fig. 16, at high beam energy the charge deposited in the silicon sensor decreases. When the charge loss effect for the floating strips is taken into account, the signal measured on the neighboring strips of a floating strip can be below threshold.

For all the above reasons, when a cluster seed is found, the read-out values of the seed and of its adjacent strips are always collected and stored.

In Fig. 17, a plot of raw ADC counts as a function of read-out channel is reported for a 70-MeV proton beam energy. The strips identified by a channel index from 4080 to 4224 are hit by the beam. The presence of two well separated signal distributions confirms charge loss for all the events for which a floating strip is hit. A profile along the Y axis (histogram in the inset) shows two clear peaks related to particles hitting either a floating (signal peaked at $\simeq$ 60 ADC) or a read-out strip (signal peaked at $\simeq$ 180 ADC).

This effect must be corrected, since released charge must be independent from the hit strip. In order to correct the difference in deposited signal, it is useful to introduce the variable η, defined for the two most significant strips (either seed or contiguous) as:

$$\eta = \frac{S_{right}}{S_{right} + S_{left}},$$

where S is the signal released on the strips, while right/left label marks the highest/lowest channel between seed and most significant

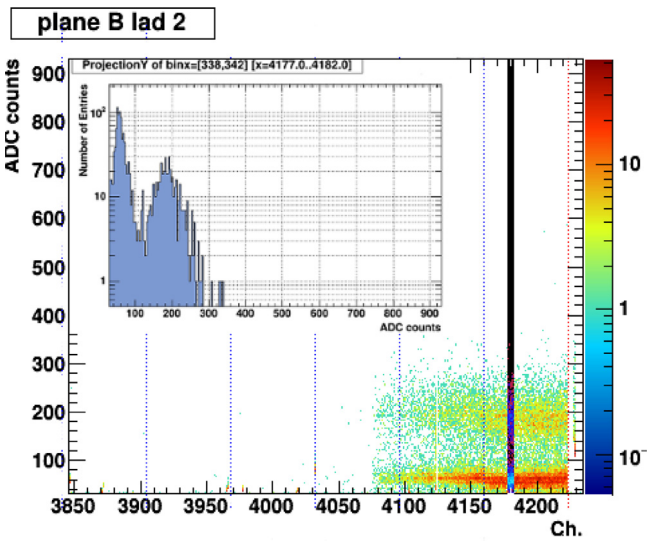

Fig. 17. Raw ADC counts as a function of read-out channel for a silicon ladder of the internal tracker plane, during a 70-MeV proton run: beam spread was such that a region of ≃ 3 cm was hit, from approximately channel 4080 to 4224. The two distributions appearing in the plot are related to particles hitting either the read-out strips (peak at 60 ADC) or the floating strips (peak at 180 ADC). A projection along the Y axis (inset), for channels 4178–4182 included in the vertical black line, clearly tells the two signals apart from each other (color online).

neighbor. Indeed, when cluster multiplicity is 1, there is a signal only in the seed, and its two neighboring strips have S-values close to zero. In this case, the adjacent strip with the highest S-value is used to calculate η, which will turn out 0 or 1 depending on the position of the chosen adjacent strip with respect to the seed.

When the particle hits a read-out strip, no charge loss can be assumed, such that the ADC read-out value can be considered correct. Fig. 18(a) shows a 2-dimensional histogram of ADC count values as a function of η for all the events in a 100-MeV proton run. Most events are concentrated at $\eta = 0$, $\eta = 0.5$ and $\eta = 1$. The profile along the Y axis (Fig. 18(b)), i.e., the mean count value in each η bin, can be fitted by a parabolic function $P(\eta)$ that can be normalized such that:

$$P(\eta = 1) = P(\eta = 0) = 1. \tag{3}$$

According to the above definition, the η-corrected deposited signal can be obtained by:

$$ADC_{corr} = \frac{ADC_{raw}}{P(\eta)}. \tag{4}$$

The η-correction effect, applied to data from the 37-MeV proton run, is illustrated in Fig. 19. The left panel (a) contains the raw signal distribution measured by one silicon ladder. The presence of two peaks mirrors the occurrence of cluster multiplicity 1 or 2. The right panel (b) shows the same plot after η-correction of the raw cluster signal on a event-by-event basis, resulting in the merging of the peak at ∼ 180 ADC counts with the one at higher energy.

5.1.3. Silicon tracker dE/dx energy calibration

Since we are dealing with particles that release just a small fraction of their energy in the tracker layers, the distribution of the energy loss is expected to be a Landau, defined as:

$$\phi(\lambda) = \frac{1}{\pi}\int_0^\infty e^{-u\ln(u)-\lambda u}\sin(\pi u)du$$

where λ is the Landau's universal variable.

To perform energy calibration, the cluster distribution recorded by the tracker for particles at each given energy was computed first. Each of these distributions, obtained after η-correction, was fitted by a Landau/Gaussian convolution

$$\phi(\lambda) * Gauss(\mu = 0, \sigma = \sigma_0),$$

with σ_0 the intrinsic charge resolution of the clusters, to take into account resolution effects on charge collection, and the resulting mean was then used for calibration (Fig. 20).

Iterating this procedure at all available energies, the $\langle ADC_{corr}\rangle$ behavior as a function of particle $\beta\gamma$ is obtained. $\langle ADC_{corr}\rangle$ distribution (which represents $\frac{dE}{dx}$) must be fitted by a Bethe-Bloch function, which describes charged particles' mean energy loss per distance traveled:

$$\langle\frac{dE}{dx}\rangle = p_0 \cdot \frac{4\pi n z^2}{m_e c^2\beta^2}\cdot(\frac{e^2}{4\pi\epsilon_0})^2\,[\ln(\frac{2m_e c^2\gamma\beta^2}{I}) - \beta^2],$$

where p_0 is a scale parameter used to adapt the function to count distribution and convert ADC counts into MeV energy loss. Fig. 21 shows a very good agreement between experimental points from proton beam data and theoretical expectation for energy loss in a ladder of the tracker. The values are different for each ladder and each side. The conversion factor used to estimate energy loss in the silicon tracker is calculated in the following way:

$$K_{ADC\to MeV} = \frac{300\mu m}{p_0},$$

where 300 μm is the thickness of each silicon ladder.

Taking as an example ladder 2, side P, as well as fit results shown in Fig. 21, the resulting conversion factor is:

$$K_{2p} = \frac{0.03cm}{10.61 \pm 0.1117\ (ADC\times cm)/MeV} = (28.3 \pm 0.3)\times 10^{-4} MeV/ADC$$

5.2. Calorimeter energy calibration

The energy calibration of the calorimeter was performed taking advantage of proton beams at Trento Proton-Therapy Center, electron beams at the Frascati BTF, and atmospheric muons. We hereby define "Upper calorimeter" the tower of plastic scintillators, that is, the upper part of the HEPD range calorimeter. The lower part is the LYSO calorimeter.

5.2.1. Upper calorimeter

Light collected by the couple PMTs placed at corners of any scintillator plane is in principle dependent on the position of the incident beam. Nevertheless, beam data analysis and MC simulations show that collected light is quite position-independent in a very large central region of the planes, far from corners and borders. Consequently, as to Upper Calorimeter, data acquired in central positions were used for energy calibration purposes.

After pedestal subtraction and equalizion of PMT signals, an offline event selection was applied. Such a selection eliminates multi-particle or scattered events, calling for lateral containment of particles in order to avoid energy leakage, and requiring a minimum number of "hit planes" to reject events with anomalously low energy loss (large scattering for electrons, nuclear interaction for protons, etc.).

For each hit plane, the signal from the plane is calculated as the sum of the two corresponding PMTs signals, with total signal released in the Upper Calorimeter being the sum of signals released in all individual hit planes.

For each energy beam, the ADC distribution of total signal is then fitted by a Gaussian function providing a mean ADC value and a sigma, while MC simulations are used to evaluate the corresponding expected energy deposition.

In Fig. 22, ADC total signal distributions for proton beams of energy 37 and 51 MeV (Fig. 22(a)), atmospheric muons (Fig. 22(b)), and a 30-MeV electron beam (Fig. 22(c)), respectively, are shown; in the electron

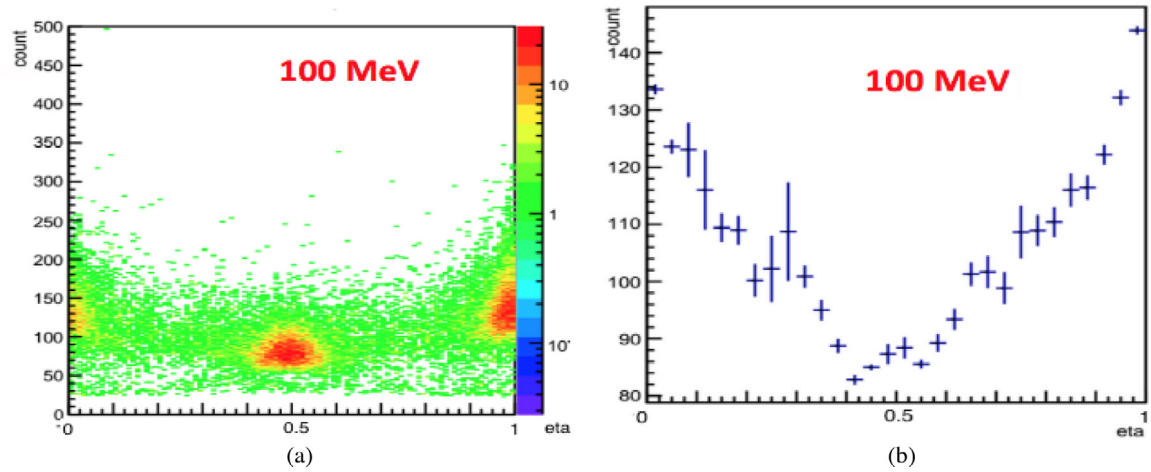

(a) (b)

Fig. 18. η-correction: (a) ADC counts vs η distribution in the central ladder (external plane) for a 100-MeV proton run. (b) Longitudinal profile of the ADC counts vs η distribution (color online).

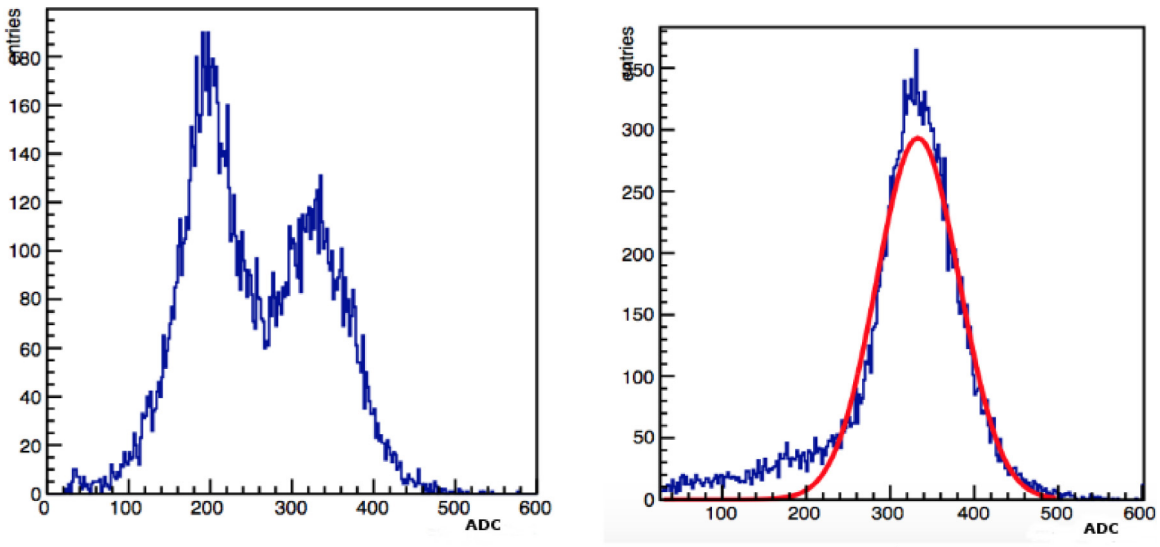

(a) (b)

Fig. 19. η-correction: (a) Number of events vs ADC counts for data in the 36-MeV proton run. The two-peak distribution is due to different hits on floating and read-out strips. (b) After applying η correction, the two peaks are merged into one centered at the "corrected" number of ADC counts, which is independent from hit position.

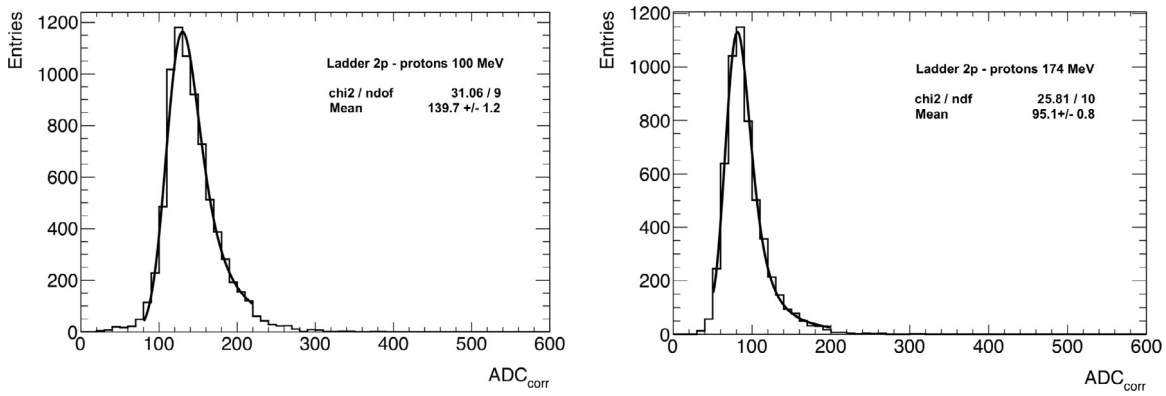

Fig. 20. Two examples of the corrected ADC counts distributions for ladder 2, side P, for 100-MeV and 174-MeV proton runs, respectively: the solid line corresponds to the fit obtained using the convolution between a Landau and a Gaussian distribution.

case, three peaks appear, corresponding to beam bunches with 1, 2, or 3 electron multiplicity, respectively (see Section 3.2.1).

The energy response function of the Upper Calorimeter, *i.e*, the ADC/MeV conversion factor, is finally obtained by linear fit of the

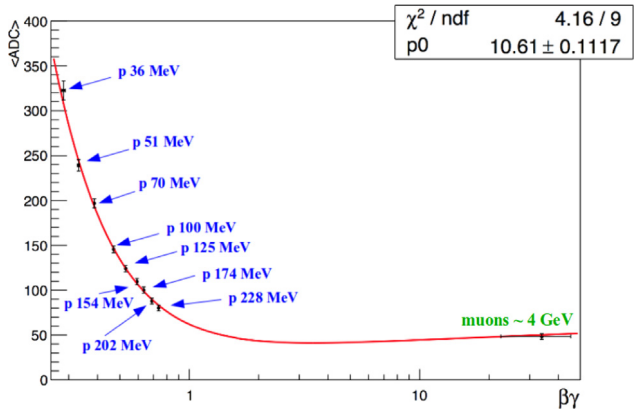

Fig. 21. Mean of ADC counts as a function of proton $\beta\gamma$ for particles hitting ladder 2, side P: the red line represents a fit performed using Bethe-Bloch function.

ADC signal peak-position vs. the expected energy deposition (in MeV) obtained by MC simulation. The resulting calibration curve, used for reconstruction of energy deposited in the Upper Calorimeter, is shown in Fig. 23; red/blue points refer to data acquired by the HOT/COLD side of HEPD electronics, respectively.

5.2.2. LYSO Calorimeter

Given the 3 × 3 LYSO matrix geometry, different beam incident positions correspond to hits on different LYSO crystals; after pedestal subtraction and equalization of PMTs, LYSO response turned out the same for all crystals.

In order to calibrate the LYSO calorimeter, large beam energies were used, corresponding to particles able to reach this forward detector ($E \geq 174$ MeV for protons, $E \geq 45$ MeV for electrons), interspersing normal acquisitions in calibration runs for electronic noise evaluation. As for the Upper Calorimeter, once the PMT signals are pedestal subtracted and equalized, an offline event selection is applied on the basis of signal-to-noise ratio in each PMT.

We applied the same offline event selection used for the Upper Calorimeter, with minimum number of hit planes equal to 16, since any particle must cross the entire Upper Calorimeter to reach the LYSO plane.

After event selection, the LYSO plane signal is calculated as the sum of signals from all individual LYSO crystals with corresponding PMTs over threshold (one PMT per crystal). The resulting ADC distribution of total signal is then fitted by a Gaussian function providing a mean ADC value and sigma, to be compared to the expected energy deposition in the LYSO plane obtained by MC simulations.

As for the Upper Calorimeter, the LYSO energy response function is finally obtained by linear fit of the ADC signal peak-position vs. the expected energy deposition (in MeV) obtained by MC simulation. The obtained calibration curve is shown in Fig. 24; red/blue points refer to data acquired by the HOT/COLD side of HEPD electronics, respectively.

5.3. Particle separation

Protons and electrons inside the detector can be easily discriminated via deposited energy and longitudinal profile.

The Bethe formula describes the mean energy loss per distance traveled by heavy charged particles (like protons) traversing matter, that is, the stopping power of the material. For lighter particles, like electrons, the energy loss is slightly different due to their small masses, indistinguishability, and much larger energy losses by Bremsstrahlung effects.

This can be appreciated in Fig. 25; bottom panels show where either protons (left) or electrons (right) lie in a plot of signal deposited in

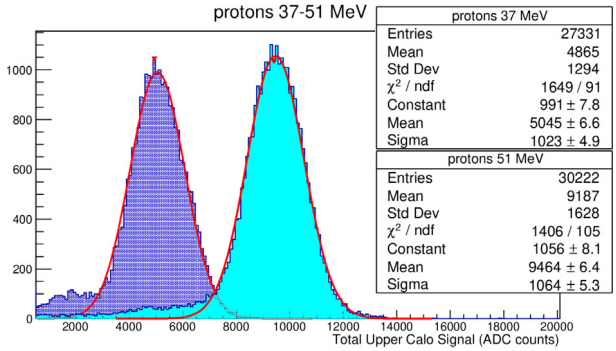

(a) 37-51 MeV protons

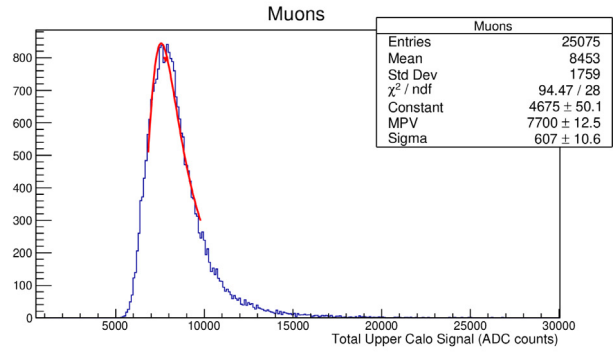

(b) Atmospheric Muons

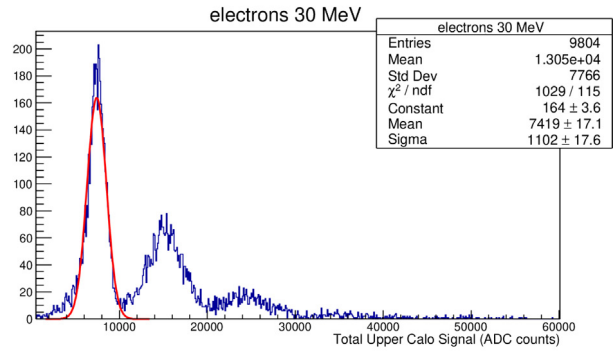

(c) 30 MeV electrons (1-2-3 electron multiplicity)

Fig. 22. Upper Calorimeter total signal distributions (HOT SIDE): (a) 37/51 MeV proton beams (blue/cyan); (b) atmospheric muons; (c) 30-MeV electron beam. (For interpretation of the references to color in this figure legend, the reader is referred to the web version of this article.)

the first plane of the scintillator tower vs. estimated particle energy; while the upper panel accommodates both distributions, highlighting how electrons (in red) populate the region with lower deposited energy with respect to protons (in blue).

Protons and electrons are also marked by different longitudinal profiles inside the calorimeter; the former present a typical rising shape followed by an abrupt decay of the signal (Bragg peak), while the latter show a more uniform profile with no sharp release in energy. This can be assessed in Figures 26 and 27, respectively, where two events from experimental data (a 125-MeV proton and a 30-MeV electron) are shown by a HEPD event-viewer.

Beam test data were used to optimize particle separation algorithms, which are currently in use for flight data.

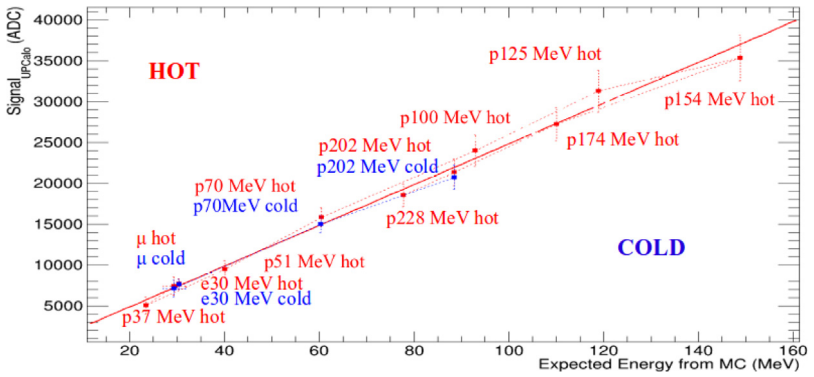

Fig. 23. Calibration curve for the HEPD Upper Calorimeter: ADC signal peak-position vs expected energy deposition (in MeV) obtained by MC simulation, providing the ADC/MeV conversion factor. Red/blue points refer to data acquired by the HOT/COLD side of HEPD electronics. For 174, 202 and 228 MeV energies, protons are not contained in the Upper Calorimeter, therefore these points "return back" along the calibration curve, that is, are found ad lower expected energies. (For interpretation of the references to color in this figure legend, the reader is referred to the web version of this article.)

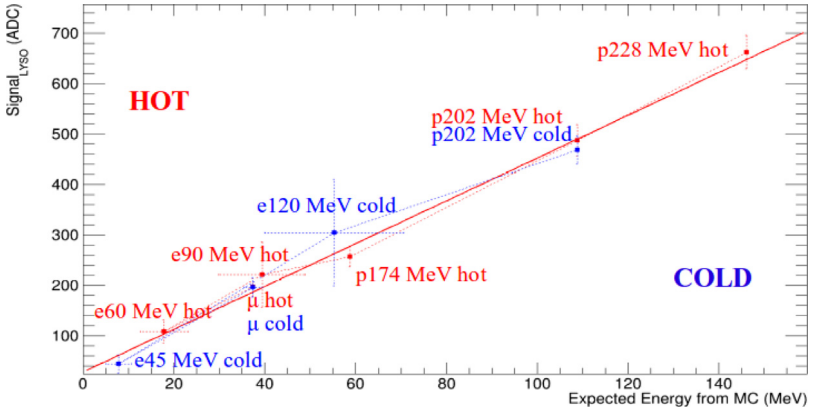

Fig. 24. Calibration curve for the HEPD LYSO plane: ADC signal peak-position vs. expected energy deposition (in MeV) obtained by MC simulation, providing the ADC/MeV conversion factor. Red/blue points refer to data acquired by the HOT/COLD side of HEPD electronics, respectively. (For interpretation of the references to color in this figure legend, the reader is referred to the web version of this article.)

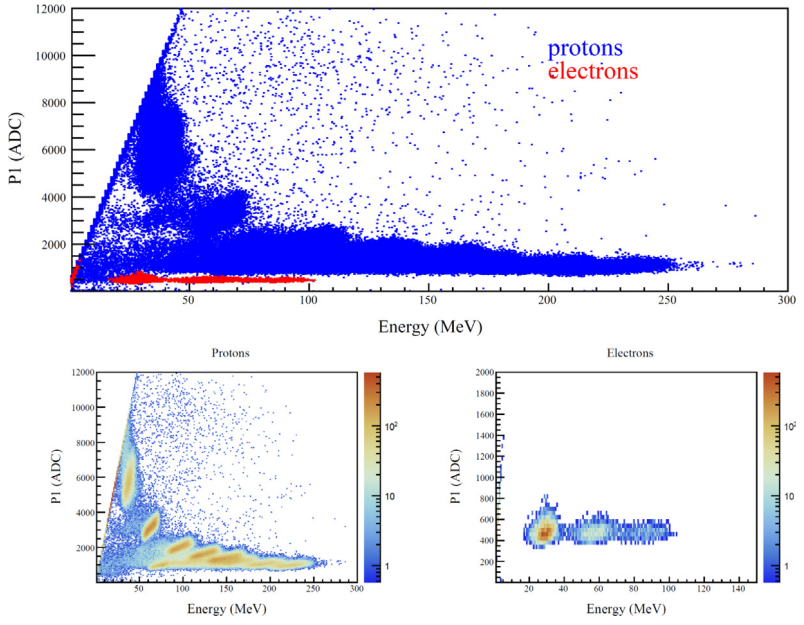

Fig. 25. Signal deposited by either protons (left bottom panel) or electrons (right bottom panel) in the first plane of the scintillator tower (P1) as a function of total energy: protons present a typical shape with higher signal at lower energies, while electrons are marked by a more uniform distribution. Both particle species populate distinct sectors of this plane (upper panel), which facilitates their discrimination. (For interpretation of the references to color in this figure legend, the reader is referred to the web version of this article.)

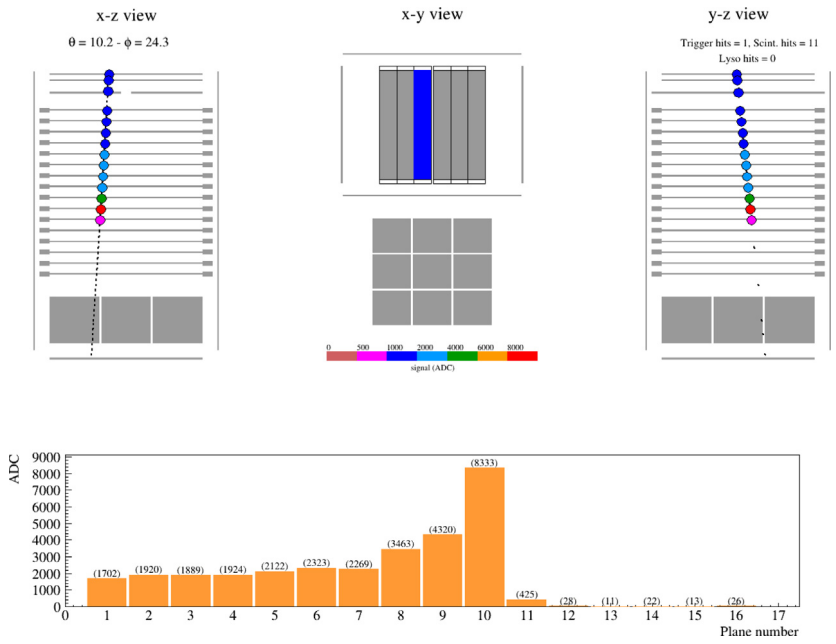

Fig. 26. Longitudinal profile of a ~ 125 MeV proton inside the scintillator tower: a Bragg peak can be clearly spotted on plane 10 (color online).

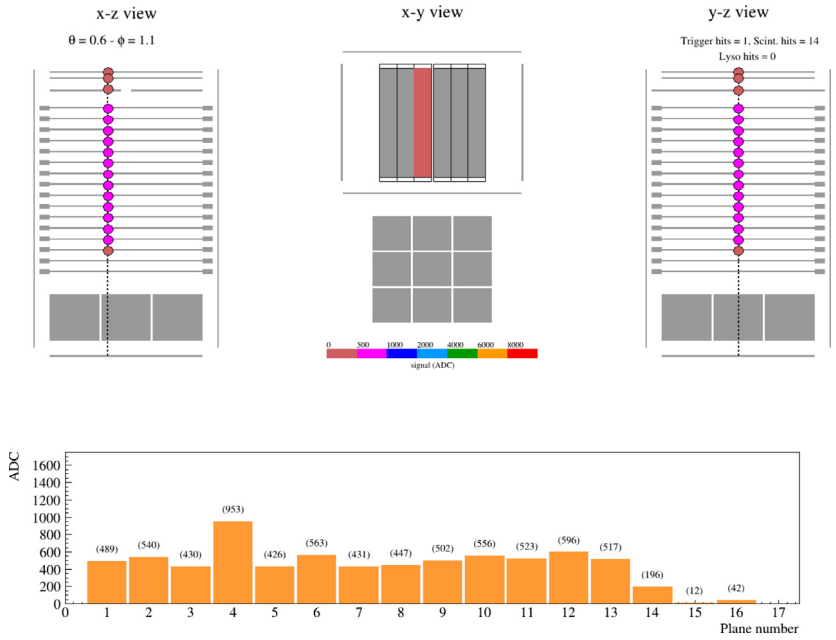

Fig. 27. Longitudinal profile of a ~ 30 MeV electron inside the scintillator tower: the signal released is almost constant along the distance traveled by the particle up to plane 14 (color online).

6. Conclusions

In this article, we have reviewed the steps needed to get a precise energy calibration of the HEPD Flight Model before launch. The silicon detector, the upper segmented scintillation calorimeter and the bottom crystal calorimeter were calibrated using beams of electrons and protons at different energies, respectively collected at the BTF (INFN National Laboratories of Frascati) and the Trento Proton-Therapy Center. Atmospheric muons – detected in clean rooms at Roma Tor Vergata Division of the National Institute of Nuclear Physics (INFN) – were exploited for additional calibration, in order to evaluate the detector response to relativistic MIP particles.

The CSES satellite was launched on February 2, 2018. On February 6, the HEPD instrument was switched on for the first time. The apparatus underwent the commissioning phase (February–July 2018), during which several on-board configurations were implemented for testing purposes; such procedures are crucial to guarantee optimal operational conditions throughout the foreseen 5-year mission duration. Since August 2018, HEPD science run has started.

CRediT authorship contribution statement

G. Ambrosi: Resources, Conceptualization, Validation. **S. Bartocci:** Data curation, Supervision. **L. Basara:** Resources, Conceptualization, Validation. **R. Battiston:** Project administration, Funding acquisition. **W.J. Burger:** Software. **D. Campana:** Writing - review & editing. **L. Carfora:** Software, Writing - original draft, Writing - review & editing. **G. Castellini:** Resources, Conceptualization, Validation. **P. Cipollone:**

Resources, Validation. **L. Conti:** Conceptualization, Formal analysis. **A. Contin:** Resources, Conceptualization, Validation. **C. De Donato:** Validation, Writing - original draft, Writing - review & editing. **F. De Persio:** Resources, Validation. **C. De Santis:** Project administration, Validation, Supervision, Methodology. **F.M. Follega:** Software, Writing - original draft, Writing - review & editing. **C. Guandalini:** Resources, Validation. **M. Ionica:** Resources, Validation. **R. Iuppa:** Software. **G. Laurenti:** Resources, Conceptualization, Validation. **I. Lazzizzera:** Supervision, Funding acquisition. **M. Lolli:** Resources, Conceptualization, Validation. **C. Manea:** Resources, Validation. **M. Martucci:** Software, Writing - original draft, Writing - review & editing. **G. Masciantonio:** Resources, Conceptualization, Validation, Methodology. **M. Mergé:** Data curation. **G. Osteria:** Resources, Conceptualization, Validation. **L. Pacini:** Software. **F. Palma:** Software, Writing - original draft, Writing - review & editing. **F. Palmonari:** Resources, Conceptualization, Validation. **B. Panico:** Software. **A. Parmentier:** Conceptualization, Formal analysis. **L. Patrizii:** Resources, Conceptualization, Validation. **F. Perfetto:** Resources, Validation. **P. Picozza:** Project administration, Funding acquisition. **M. Piersanti:** Conceptualization, Formal analysis. **M. Pozzato:** Resources, Conceptualization, Validation. **M. Puel:** Resources, Conceptualization, Validation. **I. Rashevskaya:** Resources, Conceptualization, Validation. **E. Ricci:** Resources, Conceptualization, Validation. **M. Ricci:** Supervision, Funding acquisition. **S. Ricciarini:** Project administration, Conceptualization, Validation, Methodology. **V. Scotti:** Resources, Validation. **A. Sotgiu:** Software, Writing - original draft, Writing - review & editing. **R. Sparvoli:** Project administration, Funding acquisition, Writing - original draft, Writing review & editing. **B. Spataro:** Resources, Validation. **V. Vitale:** Software. **S. Zoffoli:** Project administration, Funding acquisition. **P. Zuccon:** Resources, Conceptualization, Validation.

Declaration of competing interest

The authors declare that they have no known competing financial interests or personal relationships that could have appeared to influence the work reported in this paper.

Acknowledgments

The authors would like to gratefully thank the technical staff of the LINAC-Daphne and BTF for their fundamental support provided during the whole electron beam tests performed at INFN-LNF, Frascati, Italy.

The authors would like to gratefully thank the Trento Institute for Fundamentals Physics Applications (TIFPA) center for the support provided during the proton beam tests performed at the Proton Therapy Center in Trento, Italy.

This work was supported by the Italian Space Agency in the framework of the "Accordo Attuativo n. 2016-16-H0 Progetto Limadou Fase E/Scienza" (CUP F12F1600011005).

References

[1] X. Shen, et al., The state-of-the-art of the China Seismo-Electromagnetic Satellite mission, Sci. China Technol. Sci. 61 (5) (2018) 634.
[2] S. Alexandrin, et al., High-energy charged particle bursts in the near-Earth space as earthquake precursors, Ann. Geophys. 21 (2003) 597.
[3] V. Sgrigna, et al., Correlations between earthquakes and anomalous particle bursts from SAMPEX/PET satellite observations, J. Atmos. Sol.-Terr. Phys. 67 (15) (2005) 1448.
[4] R. Battiston, et al., First evidence for correlations between electron fluxes measured by NOAA-POES satellites and large seismic events, Nuclear Phys. B Proc. Suppl. 244 (2011) 249.
[5] E.C. Stone, A.M. Frandsen, R.A. Mewaldt, E.R. Christian, D. Margolies, J.F. Ormes, F. Snow, The advanced composition explorer, Space Sci. Rev. 86 (1998) 1–22.
[6] V. Domingo, B. Fleck, A.I. Poland, The SOHO mission: an overview, Sol. Phys. 162 (1–2) (1995) 1–37.
[7] M.L. Kaiser, T.A. Kucera, J.M. Davila, O.C.S. Cyr, M. Guhathakurta, E. Christian, The STEREO mission: An introduction, Space Sci. Rev. 136 (1–4) (2008) 5–16.
[8] R. Müller-Mellin, S. Böttcher, J. Falenski, E. Rode, L. Duvet, T. Sanderson, B. Butler, B. Johlander, H. Smit, The solar electron and proton telescope for the STEREO mission, Sol. Phys. 136 (1–4) (2008) 363–389.
[9] D. Verscharen, A step closer to the Sun's secrets, Nature 576 (7786) (2019) 219–220.
[10] M. Aguilar, et al., First result from the alpha magnetic spectrometer on the international space station: Precision measurement of the positron fraction in primary cosmic rays of 0.5-350 GeV, Phys. Rev. Lett. 110 (14) (2013) 141102.
[11] M. Duranti, et al., The AMS-02 detector on the ISS - Status and highlights, after the first 7 years on orbit, EPJ Web Conf. 209 (2019) 01014.
[12] O. Adriani, et al., The PAMELA mission: Heralding a new era in precision cosmic ray physics, Phys. Rep. 544 (4) (2014) 323.
[13] O. Adriani, et al., Ten years of PAMELA in space, Riv. Nuovo Cimento 40 (10) (2017) 473–522.
[14] A. Ambrosi, et al., The HEPD particle detector of the CSES satellite mission for investigating seismo-associated perturbations of the Van Allen belts, Sci. China Technol. Sci. 61 (5) (2018) 643.
[15] J. Lin, et al., CSES GNSS ionospheric inversion technique, validation and error analysis, Sci. China Technol. Sci. 61 (5) (2018) 669.
[16] J. Cao, et al., The electromagnetic wave experiment for CSES mission: Search coil magnetometer, Sci. China Technol. Sci. 61 (5) (2018) 653.
[17] B. Cheng, et al., High precision magnetometer for geomagnetic exploration onboard of the China Seismo-Electromagnetic Satellite, Sci. China Technol. Sci. 61 (5) (2018) 659.
[18] X. Li, et al., The high-energy particle package onboard CSES, Radiat. Detect. Technol. Methods 3 (22) (2019) 22.
[19] V. Scotti, F. Osteria, The electronics of the HEPD of the CSES experiment, Nucl. Part. Phys. Proc. 291–293 (2017) 118.
[20] P. Picozza, et al., Scientific goals and in-orbit performance of the high-energy particle detector on board the CSES, Astrophys. J. Suppl. Ser. 243 (1) (2019) 16.
[21] S. Agostinelli, et al., GEANT4: A simulation toolkit, Nucl. Instrum. Methods A506 (2003) 250–303.